An FSEI approach for the assessment of stenotic aortic valve effects on the left heart hemodynamics

Francesco Viola[a,*], Valentina Meschini[a], Roberto Verzicco[b,c,a]

[a] *Gran Sasso Science Institute, Italy*
[b] *Department of Industrial Engineering, University of Roma Tor Vergata, Italy*
[c] *PoF group, University of Twente, The Netherlands*

Abstract

Fluid-structure-electrophysiology interaction (FSEI) deals with (i) the active contraction of the myocardium, (ii) the complex blood motion and (iii) the related deformation of the cardiac tissues. This three-way coupled approach is key for obtaining predictive cardiac information as the tissue kinematics comes as a part of the solution, rather than being imposed as a boundary condition. FSEI is here applied to study the effects induced by aortic valve stenosis on the hemodynamics. This pathology, typically occurring in elderly individuals, is caused by the stiffening of the valve leaflets, thus impairing the valve functioning and reducing the pumping efficiency of the heart. The disease severity is gradually increased within a high-fidelity model for the left heart, while keeping the same geometrical, elastic and electrophysiological properties of the cardiac system, which would be impossible with *in-vivo* experiments. We observe an increase of the transvalvular pressure drop and of the peak velocity of the systolic jet velocity along with a reduction of the cardiac ejection fraction. Furthermore, a stenotic aortic valve significantly alters the wall shear stresses and their spatial distribution over the aortic arch and valve leaflets, which may induce a remodelling process of the ventricular myocardium. The numerical results from the multi-physics model are fully consistent with the clinical experience, thus further opening the way for computational engineering aided medical diagnostic.

*Corresponding author
Email address: francesco.viola@gssi.it (Francesco Viola)

Keywords: Hemodynamics, fluid-structure interaction, aortic stenosis

1. Introduction

The heart is a vital organ whose functioning results from the complex interaction between electrophysiology, tissue mechanics and hemodynamics. Despite its remarkable reliability, some of its parts can deteriorate in time, especially on the left side that feeds the systemic circulation and supports the highest pressure differences [1]. Valvular heart disease accounts for ∼15% of all cardiac surgical procedures in the western Countries and approximately two thirds of them are for aortic valve replacement owing to aortic stenosis (AS) disease [2]. Valves stenosis occurs whenever the valve leaflets stiffen, thus impairing their normal operation yielding an increased risk of myocardial infarction and mortality [3, 4, 5]. In particular, the prevalence of moderate to severe aortic stenosis is above 2% for patients older than 65 years and it exceeds 4% for those older than 75 years [6]. More specifically, the calcific aortic stenosis is the most common cause of aortic valve disease afflicting 2-3% of the North American population aged over 65 years [7]. Furthermore, these data are projected to more than double by 2050 in the developed Countries [8].

The degree of stenosis associated with the symptoms varies among patients and in most cases AS can now be diagnosed before symptoms onset through physical examination and echocardiography. The latter has become the standard approach for the diagnosis and evaluation of valve disease since it allows the accurate definition of valve anatomy, including the cause and the severity of AS. Grading the AS severity is, indeed, important to predict the patient clinical outcome. To this aim the European Association of Echocardiography (EAE) together with the American Society of Echocardiography (ASE) [9] propose to measure the AS severity using a combination of parameters such as the aortic valve area (AVA), the velocity of the systolic jet and the mean transvalvular pressure drop (TPD). In particular, *mild* AS is characterized by an aortic jet velocity comprised between 2.0 and 2.9 m/s, a mean TPD below 20 mmHg and

an AVA of 1.5 to 2.0 cm^2. The case of an aortic jet velocity of 3.0-3.9 m/s, a mean TPD equal to 20 to 39 mmHg and an AVA in between 1.0-1.5 cm^2 is recognized as *moderate* AS. Finally, *severe* AS entails a more significant obstruction to LV outflow usually resulting in an aortic jet velocity exceeding 4 m/s, a mean TPD of at least 40 mmHg along with an AVA smaller than 1.0 cm^2, which is about 25% the corresponding value in the healthy case. These guidelines are used to quantify the severity of the AS and obtain an empirical prediction of the temporal evolution of the disease. As an examples, it has been observed that in most patients with mild AS, a worsening of the calcification yielding severe AS occurs in typically 5-10 years [9].

A deeper understanding of the basic mechano-biologic mechanisms leading to valve dysfunction are needed to optimize medical interventions and prevent the disease progression. In this spirit, Computational Engineering is becoming an added value in medical research since it provides a framework to study the alterations caused by heart pathologies and to predict the most favorable medical treatment. Numerical simulations allow, indeed, to run ideal experiments and provide a complete access to hemodynamics data, which is unattainable through in-vivo experiments. For instance, the rate of calcification of both tricuspid (normal) and the bicuspid (pathologic) aortic valves has been investigated employing structural finite-element simulations of the valve leaflets [10]. On the other hand, the initiation and growth of calcifications has been studied re-creating numerically the different calcification growth stages observed in patient-specific tomographic scans [11]. A patient-specific computational model to quantify the biomechanical interaction between the transcatheter aortic valve (TAV) stent and the stenotic aortic valve during TAV intervention has been developed to plan pre-operative strategies and facilitate next generation device design [12, 13]. Several works then focused on the complex fluid-structure-interaction (FSI) governing the opening and closing dynamics of the aortic valve leaflets in physiological conditions in the case of biological [14, 15] and mechanical [16, 17] prosthetic valves. More recently the FSI of calcific aortic valves has been solved both using an Arbitrary Lagrangian-Eulerian (ALE) method [18]

and an immersed boundary approach [19]. In the latter study, the aorta was modelled as a curved rigid pipe with a 180 turn and three different stenoses with area reductions were considered in the analysis.

In all these FSI studies, however, the pulsatile flow in the aorta was driven by imposing an unsteady inflow at the aortic orifice and the computational domain only comprises the thoracic aorta, thus overlooking the left ventricle and atrium whose dynamics generates the unsteady inflow itself. The hemodynamics in the aorta and in the left heart are intrinsically coupled owing to the elliptic nature of the governing (Navier-Stokes) equations and only considering the whole left heart hemodynamics allows to solve the transvalvular pressure drop, which is a clinical quantity of paramount importance to quantify AS, as introduced above. In this work we present a numerical approach based on FSEI to study the AS and its effects on the hemodynamics accounting for the whole left-heart functioning, including the electrical activation of the myocardium. As a consequence, the valve leaflets kinematics along with the inflow through the valvular orifices induced by the heart chambers expansion/contraction are not imposed but are obtained as a part of the numerical results. The hemodynamics of the whole system is thus investigated comparing healthy to pathological conditions to highlight the alterations of the ventricular flow produced by the AS, which is incorporated by penalising the mobility of the aortic valve leaflets. Specifically, the severity of the AS can be progressively increased from moderate to acute, according to the current risk stratification [20]. The relevant clinical parameters introduced above to assess AS severity such as the AVA, the systolic jet velocity and mean TPD are measured numerically and validated against clinical observations before studying the wall shear stresses (WSS), which can not be measured in-vivo directly.

The paper is structured as follows. In Section 2 the problem configuration and the AS model are presented along with the FSEI computational framework. The results on the hemodynamics alteration induced by AS are shown in Section 3 and compared against an healthy valve configuration. Closing remarks and perspectives for future studies are given in the final Section 4.

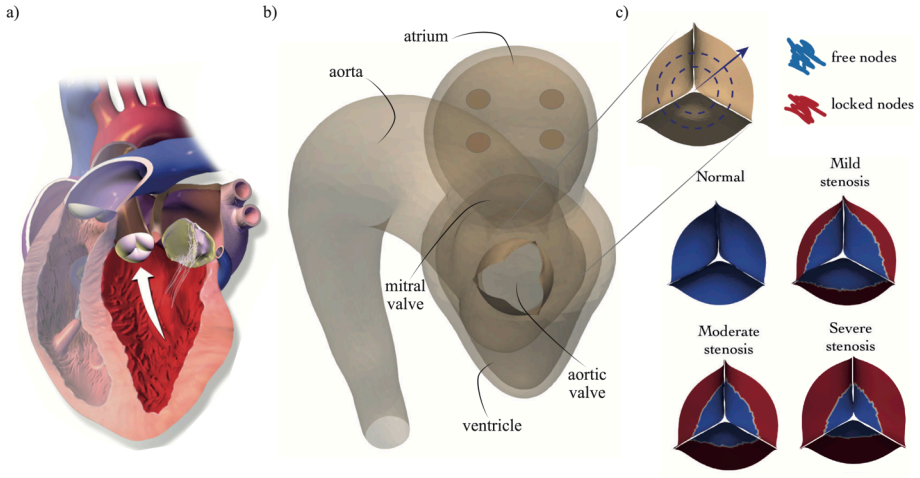

Figure 1: a) Sketch of the heart highlighting its left pump and corresponding b) left heart geometry used in the computational model comprising ventricle, atrium, thoracic aorta, mitral and aortic valve. c) Reduced mobility regions of the aortic valve leaflets according to the AS model, the blue region indicate healthy tissues whereas the red one calcified tissues.

2. Materials and methods

2.1. Problem configuration and aortic stenosis modelling

Let consider the left heart geometry shown in Figure 1 which reproduces the main geometrical features of the cardiac anatomy as depicted in the medical atlas. It comprises a left atrium and a left ventricle with a free-stress volume of 40 ml and 125 ml, respectively [1]. The left atrium receives oxygenated blood via four circular inlets corresponding to the inlets of the pulmonary veins and is connected to the left ventricle through the mitral valve, which is made of two leaflets (anterior and posterior) modelled as deformable membranes 2 mm thick mounted on a mitral orifice of diameter $d_m = 24$ mm. During systole the left ventricle contracts and pumps blood through the ascending aorta that bends down 180° in the aortic arch and then extends in the thoracic descending aorta. The ventricle and the aorta are connected by the aortic valve that is made of three cusps placed just before the Valsalva sinuses, with the three leaflets modelled as deformable membranes of thickness 1.5 mm. The Reynolds number

is defined using as reference length and velocity, the diameter of the atrial orifice ($d_a = 20$ mm) and the orifice averaged velocity of the aortic jet during systolic peak ($U_a = 1.5$ m/s, see table 1) corresponding to $Re = U_a d_a/\nu = 6250$, with $\nu = 4.8 \times 10^{-6}$ m^2/s the effective kinematic viscosity for human blood with an hematocrit of 40% (Newtonian blood model) [21].

As mentioned above, the AS depends on the deterioration of the tissues owing to a calcification process yielding a local stiffening over the leaflets, thus reducing their elasticity and mobility. In order to reproduce such reduced mobility, AS is modelled by blocking a certain region of the leaflets next to the aortic root (indicated by the red area in Figure 1c) to its initial position as a function of the disease severity, which can be progressively varied from moderate to acute by increasing the calcific area. A similar approach was adopted to model effectively the mitral valve stenosis in previous FSI numerical simulations [22]. Here, we have focused on four different cases: a *normal* valve corresponding to healthy conditions in which the valve leaflets can open freely according to the hydrodynamic loads; a *mild* stenosis, in which only 30 % of the orifice area is blocked; a *moderate* stenosis where 55% of the leaflet area is blocked and a *severe* stenosis corresponding to a calcific obstruction of 80 % the aortic orifice area. Aside the AS modelling, the same cardiac configuration in both healthy and pathologic cases is considered in order to better enlighten the role of the AS severity. Specifically, the same free–stress geometry of heart chambers and veins is used, along with the same elastic and electrophysiology properties of the myocardium.

2.2. Numerical method: Fluid-Structure-Electrophysiology interaction (FSEI)

Building a computational model of the heart entails dealing with the complex fluid-structure interaction between the pulsatile hematic flow and the deforming biological tissues whose active contraction is triggered by the electrophysiological system. Our group has developed a computational framework for solving the full FSEI that has been extensively discussed and validated in previous studies [23, 24] and which is only briefly summarized here.

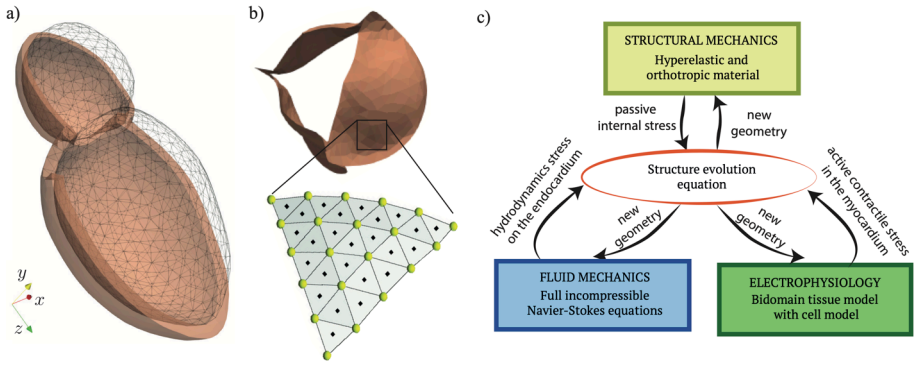

Figure 2: Snapshots of a) the 3D myocardium with the corresponding 2D endocardium and of b) the 2D aortic valve. The inset in b) shows a sketch of the Lagrangian markers (black dots) distributed over 2D triangulated meshes. c) Schematic of the fluid-structure-electrophysiology (FSEI) interaction with the three solvers coupled through the equation for the structural dynamics (4).

As shown in Figure 2a, a three-dimensional (3D) solver is used for the ventricular and atrial myocardium which are meshed using a tetrahedral mesh, with the endocardium wet by the blood corresponding to a triangular inner surface. On the other hand, thin membranes as the valve leaflets and the aorta are discretized through two-dimensional (2D) triangulated surfaces (see Figure 2b). The dynamics of the deformable heart tissues is thus solved using a spring-network structural model based on the Fedosov's interaction potential approach [25, 26] where the mass of the tissues is concentrated at the mesh nodes and an elastic spring is placed at each mesh edge connecting two nodes. The anisotropic and hyperelastic nature of biological cardiac tissues is modelled by a larger elastic stiffness in the fiber direction, $\hat{\mathbf{e}}_f$ than in the sheet $\hat{\mathbf{e}}_s$ and sheet-normal $\hat{\mathbf{e}}_n$ directions and by a nonlinear strain-stress behaviour according to a Fung-type constitutive relation, where the strain energy density reads:

$$W_e = \frac{c}{2}(e^Q - 1), \tag{1}$$

with $Q = \alpha_f \epsilon_{ff}^2 + \alpha_s \epsilon_{ss}^2 + \alpha_n \epsilon_{nn}^2$ being a combination of the Green strain tensor components in the fiber, ϵ_{ff}, sheet, ϵ_{ss}, and sheet-normal ϵ_{nn} directions. In the 2D case, the bending stiffness of the tissues is accounted for by introducing

an additional bending energy potential $W_b = k_b[1 - \cos(\theta - \theta_0)]$ among two mesh faces sharing an edge, with θ_0 (θ) their relative free-stress (instantaneous) inclination [27] and the elastic model parameters have been set as in [24].

The left heart is immersed in a Cartesian Eulerian mesh of size $l_x \times l_y \times l_z = 120 \times 120 \times 60$ mm^3 and during the cardiac dynamics blood can be sucked from the outer volume through the inlets of the pulmonary veins or propelled towards the same outer volume through the aorta. The no-slip condition on the wet heart tissues is imposed using an immersed boundary technique based on the moving least square (MLS) approach [28, 26]. In the case of hematic flows in the heart chambers and/or main vessels, the blood can be modelled as a Newtonian fluid and governing incompressible Navier-Stokes and continuity equations read:

$$\begin{aligned} \frac{\partial \mathbf{u}}{\partial t} + \mathbf{u} \cdot \nabla \mathbf{u} &= -\nabla p + \frac{1}{Re} \nabla^2 \mathbf{u} + \mathbf{f}, \\ \nabla \cdot \mathbf{u} &= 0, \end{aligned} \tag{2}$$

where $\mathbf{u}$ and p are the blood non-dimensional velocity and pressure and Re is the Reynolds number as defined in section 2.1. The body force $\mathbf{f}$ is used to impose the boundary condition at the interface within the immersed boundary context. The equations (2) are solved numerically using a DNS solver based on central second-order finite-differences discretized on a staggered mesh [29, 24]. In order to provide the hydrodynamic loads as input to the structural solver for fluid-structure coupling, the pressure and the viscous stresses are evaluated at the Lagrangian markers laying on the immersed body surface as $\mathbf{F}_f^{ext} = [-p_f \mathbf{n}_f + \boldsymbol{\tau} \cdot \mathbf{n}_f] A_f$, being A_f the area of the triangular face and $\mathbf{n}$ its normal direction.

An Eulerian grid of $257 \times 257 \times 343$ nodes evenly distributed in all three directions is used for the simulations, which has been seen to correctly reproduce the intraventricular hemodynamics and the mitral valve dynamics [24]. The code is GPU accelerated and relies on the CUDA Fortran library [30]. The wall-clock time per time step using a single node (equipped with four Nvidia-V100 devices) of the GPU cluster Marconi100 by Cineca is 0.115 s. Since half

of a million of time steps are needed to integrate a single heartbeat at 60 bpm, the code has been run for 4 days in order to integrate 3 millions timesteps and solve 6 heart beats. The results are then phase-averaged over the last 5 heart beats, thus discarding the first one.

The electrical activation of the myocardium is governed by the bidomain model, called in this way because the conductive media is modelled as an intracellular and an extracellular overlapping continuum domains that are separated by the myocytes membrane [31, 32]. The potential difference across the membrane of the myocytes, v the transmembrane potential, and the extracellular potential, v_{ext} extracellular potential, satisfy:

$$\begin{aligned} \chi\left(C_m\frac{\partial v}{\partial t}+I_{ion}(\boldsymbol{\eta})+I_s\right) &= \nabla\cdot(\mathcal{M}^{int}\nabla v)+\nabla\cdot(\mathcal{M}^{int}\nabla v_{ext}),\\ 0 &= \nabla\cdot(\mathcal{M}^{int}\nabla v+(\mathcal{M}^{int}+\mathcal{M}^{ext})\nabla v_{ext}),\\ \frac{\mathrm{d}\boldsymbol{\eta}}{\mathrm{d}t} &= F(\boldsymbol{\eta},v,t) \end{aligned} \tag{3}$$

where χ and C_m are the surface-to-volume ratio of cells and the membrane capacitance. The parameters $\mathcal{M}^{int}$ and $\mathcal{M}^{ext}$ are the conductivity tensors of the intracellular and extracellular media, which reflect the orthotropic myocardium electrical properties with the electrical signal propagating faster along the muscle fiber than in the cross-fibers directions [32, 24]. The quantity I_{ion} is the ionic current per unit cell membrane that is prescribed by the ten Tusscher-Panfilov model [33] cellular model, which is indicated by the last equation and is made by a system of 19 ordinary differential equations with unknown state vector $\boldsymbol{\eta}$. The external triggering stimulus I_s initiates the myocardial depolarization and, since the sinoatrial node that is placed in the upper part of the right atrium is not included in the computational domain, localized I_s are prescribed with the appropriate delays at the Bachmann and His bundles for the left atrium and ventricle, respectively. The heart rate (HR) is imposed as an input parameter of the cardiac configuration by prescribing the time interval between two consecutive spikes of I_s. Since the HR is seen to be weakly affected by the aortic stenosis (in [34] the mean HR was seen to decrease by -2.8 bpm in the case of

AS) the same HR of 60 bpm is imposed in both the healthy and pathological cases in order to better ascertain pathologic effects of the AS on the hemodynamics.

The set of equations 3 are discretized on the same tetrahedral mesh used for the three-dimensional structural solver by using an in-house finite volume (FV) library, which provides a suitable approach for solving the electrophysiology equation in complex geometries. The active muscular tension $\mathbf{F}_n^{act}$ at the mesh cell is then obtained as a function of the transmembrane potential v through the model equation proposed by [35].

The contraction and relaxation of the heart chambers along with the aorta and valve leaflets kinematics results from the dynamic balance between the inertia of the tissues, the external hydrodynamic forces given by the fluid solver $\mathbf{F}_n^{ext}$, the internal passive forces from the structural solver $\mathbf{F}_n^{int}$ and the active tension computed by the electrophysiology solver $\mathbf{F}_n^{act}$:

$$m_n \frac{\mathrm{d}^2 \mathbf{x}_n}{\mathrm{d}t^2} = \mathbf{F}_n^{ext} + \mathbf{F}_n^{int} + \mathbf{F}_n^{act}, \tag{4}$$

where $\mathbf{x}_n$ is the (instantaneous) node position and m_n its mass. The hydrodynamics force is non-zero only on the mesh nodes belonging to the wet surfaces (namely the valve leaflets and the inner wall of the chambers), whereas the active tension can be non-zero only for the nodes belonging to the muscular myocardium, i.e. the ventricle and the atrium. The equation of the structural dynamics (4) is integrated twice in time to determine the instantaneous tissue configuration at each time step. The new geometry can then be used as input for the fluid and electrophysiology to integrate the corresponding governing equations to obtain the new active and external forces acting, in turn, on the tissues, as indicated in Figure 2c. As detailed in [24] both a strong and loose coupling approaches have been implemented in the code. We recall that in this cardiac model the instantaneous chambers volume and the pulsatile flow in the aorta are not imposed as boundary conditions but come as a part of the FSEI solution.

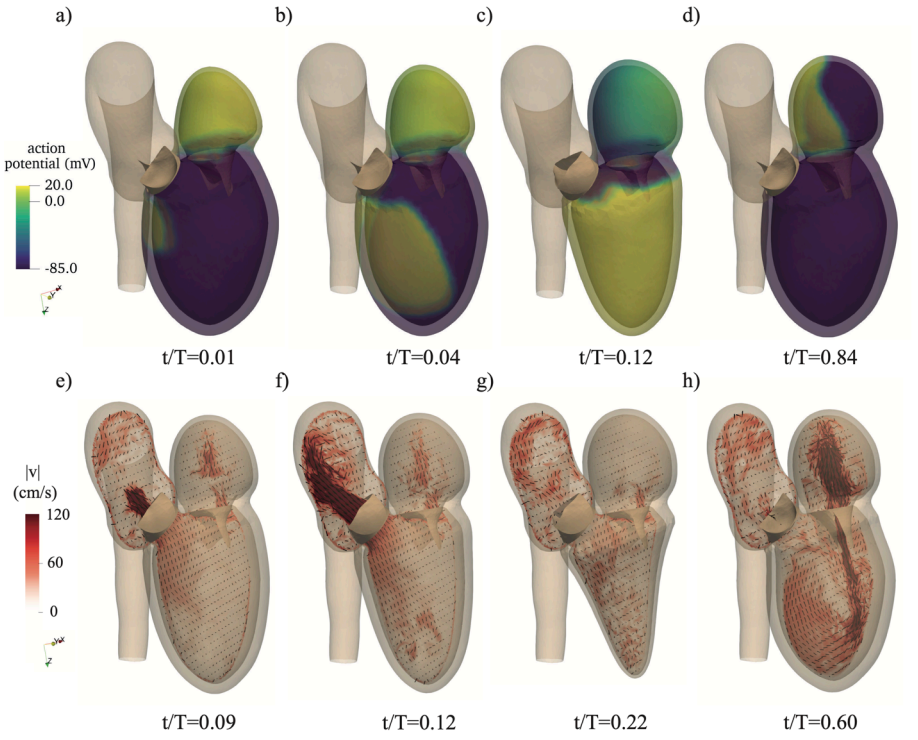

Figure 3: Cardiac dynamics in the healthy case. a-d) Snapshots of the transmembrane potential propagation in the left heart, with T the heart beating period. e-h) Isocontours of the instantaneous velocity magnitude with superimposed velocity vectors (displaying one velocity vector each 36 grid points).

3. Results

In this section the effects of AS on the left heart flow in terms of hemodynamics, pressure and wall shear stresses are investigated. The healthy configuration with a normal aortic valve of AVA 2.6 cm^2 will be considered in addition to three stenotic cases of increasing disease severity corresponding to (i) mild AS with an AVA of 1.8 cm^2, (ii) moderate AS with an AVA of 1.1 cm^2 and (iii) severe AS with an AVA of 0.5 cm^2.

3.1. Hemodynamics with a healthy aortic valve

Before focusing on the effects of AS on the cardiac hemodynamics, we briefly discuss the case of normal aortic valve that will serve as a reference to better

assess the alterations produced by the stenotic pathology.

Figure 3a-d shows the electrical activation of the left heart. Initially, the myocytes are polarized and the transmembrane potential has the negative value of about -90 mV corresponding to the blue isocontour. As the electrical impulse is applied at the His bundle (panel 3a) the neighbouring ventricular myocytes depolarize and reach the positive transmembrane potential of 20 mV. This local depolarization results in a propagating wavefront quickly travelling across the tissue (panel 3b) and after about 100 ms the whole ventricle is electrically activated (panel 3c). A second electrical impulse is originated at the Bachman bundle (Figure 3d), and the electrical signal propagates along the atrial muscle causing the cells to locally change the transmembrane potential.

The action potential propagating through the atrial and the ventricular myocardium causes the contraction of the muscular fibers which, while shortening, induce a complex hemodynamics within the heart chambers. Figure 3e-h shows the hematic flow in the symmetry plane $(x - z)$ for representative instants of the heart beat. The blood flows from the upper chamber (the atrium) down to the ventricle that is the main active pump of the heart, further propelling the blood in the aorta towards the systemic circulation. Owing to the incipient ventricular contraction, pressure rises at early systole and, when it becomes larger than that of the aorta, the aortic valve opens and blood flows to the aorta (Figure 3e). As the contraction strengthens, the ejected flow rate further increases, thus fully opening the aortic valve leaflets and reaching the maximum blood velocity within the aortic jet (see Figure 3f). When the systole ends (see Figure 3g), the ventricular volume is minimum (end-systolic volume) and its myocytes start to repolarize. Consequently, the active tension decays yielding the ventricular pressure to decrease and, in turn, the aortic valve closes. Figure 3h shows as during early diastole the ventricle relaxes and the blood flow accelerates through the mitral orifice, thus opening the valve and producing a strong mitral jet (E-wave). The mitral jet then slows down during diastasis before another fluid injection generated by the atrial systole creates a second weaker mitral jet (A-wave). These last two phases of the diastole are not re-

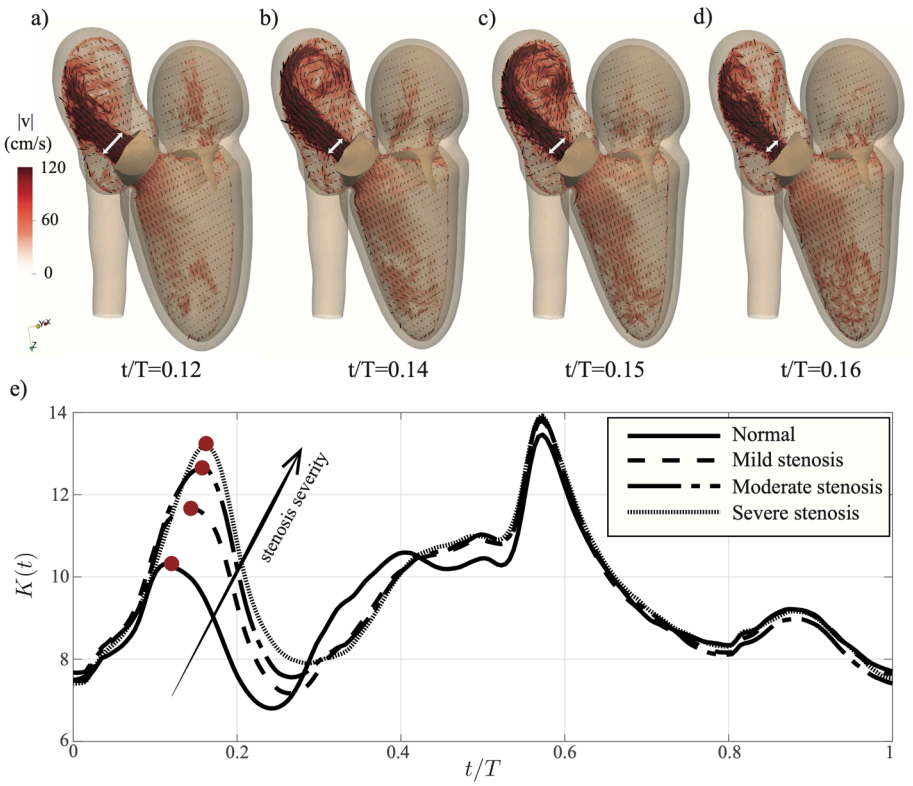

Figure 4: Isocontours of the instantaneous velocity magnitude with superimposed velocity vectors at peak systole for a) normal valve and b) mild c) moderate d) severe AS. For the sake of clarity, only 1 velocity vector every 36 grid points is shown. e) Phase-averaged nondimensional kinetic energy of the flow integrated over the left heart domain as a function of time normalized by the heart beating period. The red dots indicating the peaks of the systolic kinetic energy correspond to the hemodynamics snapshots shown in a-d.

ported here as our investigations will mainly focus on the systole, see [24] for more results on the diastole for a healthy patient.

3.2. Hemodynamics with a stenotic aortic valve

Although the basic flow features are maintained when the aortic valve leaflets get calcified, some significant alterations emerge during systole. Figure 4a-d compares the aortic jet at the peak systole for the three stenotic cases against the reference configuration corresponding to the normal aortic valve. It results

that as the AS severity increases, the systolic jet becomes more intense and its section decreases owing to the reduced mobility of the valve leaflets. Consequently, stronger upward velocities in the aorta take place as indicated by the instantaneous velocity vector (black arrows). Furthermore, the white arrow in the same panels indicates that the diameter of the aortic jet reduces significantly as the AS progresses from moderate to severe, accordingly with the reduction of the AVA. These features are more evident in the severe stenotic case (panel d) where the aortic jet is the narrowest and violently impinges over the inner wall of the aorta.

These hemodynamics alterations due to the stenotic disease also alter the integral kinetic energy per unit mass of the flow, which in nondimensional form reads:

$$\mathrm{K}(t) = \frac{1}{2} \int_{V(t)} \mathbf{u} \cdot \mathbf{u} \, \mathrm{d}V, \tag{5}$$

where the volume $V(t)$ comprises the left ventricle, atrium and aorta. Figure 4(e) shows that in all cases three energy peaks appear, where the first one ($0 < t/T < 0.3$) corresponds to the systole and it is generated by the intense velocities at the aortic outflow. The second one ($0.35 < t/T < 0.7$) is due to the diastolic filling of the ventricle owing to the relaxation of the myocardium (E-wave), whereas the latter smaller one ($0.85 < t/T < 1$) is generated by flow acceleration dueing atrial systole (A-wave). As the AS of the aortic valve gets more severe, higher values of kinetic energy within the systolic peak are observed, whereas the energy peaks occurring during the diastole are unaltered as the diastolic phase is weakly affected by the AS pathology. In particular, the maximum kinetic energy with respect to the base level (equal to about 7.4 in nondimensional unit) that is indicated by the red dots increases by 45% for mild stenosis and by 85% for severe stenosis with respect to the case of normal aortic valve. This result is explained by recalling that the aortic jet accelerates as the aortic orifice is occluded by the leaflets calcification. Hence, its maximum velocity at peak systole increases from 1.5 m/s in the healthy case to 2.6 m/s for mild stenosis, to 3.3 m/s for moderate stenosis until attaining 4.9 m/s in the case

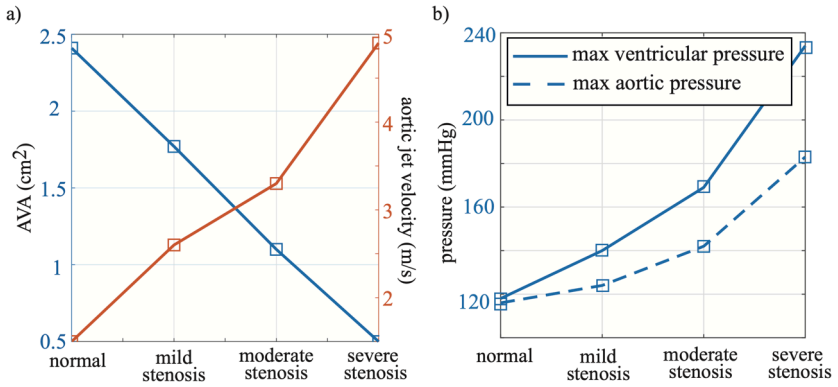

Figure 5: a) Aortic valve area (AVA) and aortic jet velocity at peak systole as a function of the AS severity. b) Maximum ventricular and aortic pressure over systole as a function of the AS severity.

of severe stenosis (i.e. more than three times the normal case, see Figure 5a). This speed-up of the aortic jet, however, is not beneficial for the cardiac flow because it is known to be associated with stronger turbulent fluctuations that may activate hemolysis and produce larger transvalvular pressure drops [36, 37].

The velocity vectors at the peak systole are also reported in Figure 6a-d now superimposed to the instantaneous pressure field for (a) normal aortic valve along with (b) mild (c) moderate and (d) severe stenosis configurations. As the stenosis gets more severe, the ventricular pressure increases from 118 mmHg observed in the healthy case to 140 mmHg for mild stenosis to 169 mmHg for moderate stenosis until reaching 234 mmHg for severe stenosis (see also Figure 5b). According to the Laplace law, as the intra-ventricular pressure increases the myocardium wall tension increases proportionally, which may induce long term consequences including heart remodelling [38] as discussed in section 4.

Since the thoracic aorta and ventricle are connected through the aortic orifice during systole, also the pressure in the thoracic aorta is altered by the stenotic disease. Figure 6e-h shows the Wiggers' diagram, which is a standard representation of the heart functioning, typically reported in the medical atlas, showing

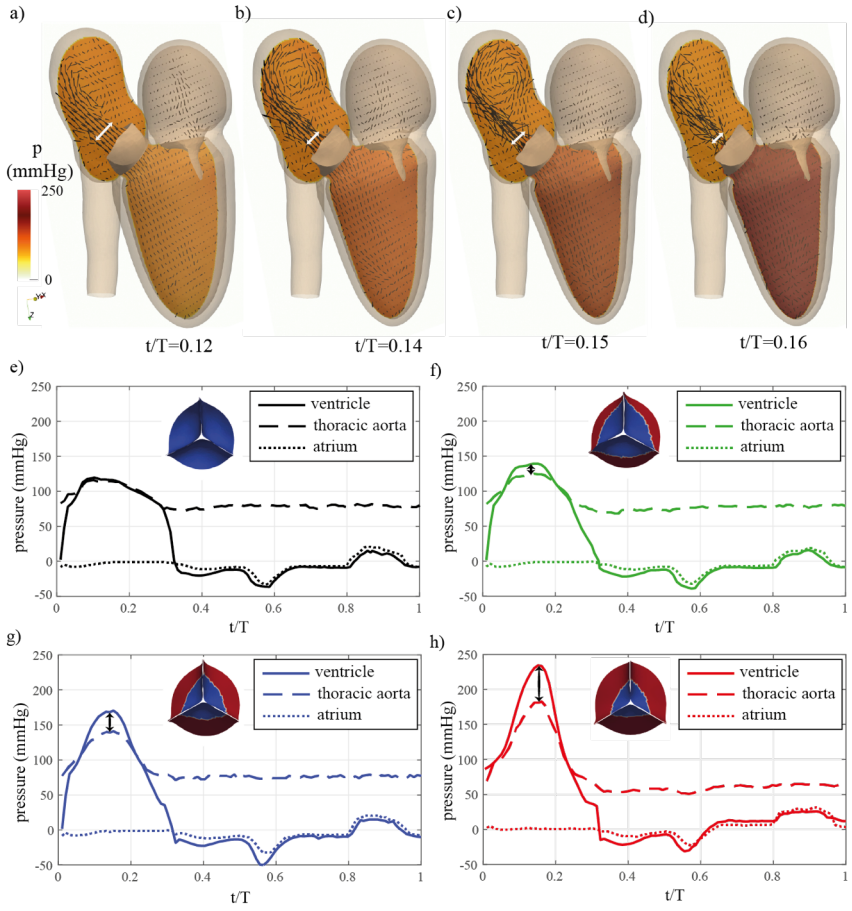

Figure 6: Isocontours of the instantaneous pressure with superimposed velocity vectors at peak systole for a) normal valve and b) mild c) moderate d) severe AS. Wiggers' diagram (see text) for e) normal valve and f) mild g) moderate h) severe AS.

the time evolution of the left cardiac pressures. The first peak ($0 < t/T < 0.3$) corresponds to the overpressure originated by the ventricular systole, whereas the latter smaller one ($0.85 < t/T < 1$) to the atrial systole. The aortic pressure (dashed line in all panels) has a baseline of about 80 mmHg when the aortic valve is closed (thus uncoupling the two chambers) and increases when the aortic valve opens during systole. In particular, at early systole $t/T < 0.05$ although the aortic valve is still closed, the aortic pressure increases owing to the in-

	aortic jet velocity (m/s)		mean transvalvular pressure (mmHg)		aortic valve area (cm^2)		ejection fraction SV/EDV
	in-vivo	numerics	in-vivo	numerics	in-vivo	numerics	numerics
Normal	<2.0	1.5	< 5	2.2	> 2.0	2.6	51%
Mild	2.0-2.9	2.6	5-20	12.7	1.5-2.0	1.8	47%
Moderate	3.0-3.9	3.3	20-40	26.4	1.0-1.5	1.1	41%
Severe	≥ 4.0	4.9	> 40	42.5	< 1.0	0.5	38%

Table 1: Comparison in the classification of aortic stenosis severity between clinical standards [39, 9] and present numerical results. The acronyms SV and EDV stands for stroke and end diastolic volume, respectively.

creasing ventricular pressure, which deforms the aortic valve leaflets which start opening. As the stenosis level is progressively increased, also the peak systolic pressure in the aorta increases from 116 mmHg measured for normal valve to 124 mmHg for mild AS to 142 mmHg for moderate AS and attains 183 mmHg for severe AS, see 5b. Still, according to the Laplace law, the transmural stresses in the aorta increase linearly with the inner pressure in the artery.

It should be remarked that not only the systolic pressures in the ventricle and in the atrium increase, but so does their difference corresponding to the TPD, which is a relevant parameter commonly used in the clinical practice to quantify the AS. A mean TPD during systole below 5 mmHg is generally associated to physiological conditions and to a smooth aortic jet, in agreement with the Wiggers' diagram in the healthy case, see Figure 6e, corresponding to a mean TPD of 2.2 mmHg. The same pressure loss raises to 12.7 mmHg in the case of mild stenosis and to 26.4 mmHg for moderate stenosis. In the configuration of severe AS a mean TPD of 42.5 mmHg is measured, which may yield to life threatening conditions in the long term.

All these relevant quantities for the cardiac functioning have been obtained from the multi-physics model and reported in Table 1. Specifically, the (i) the maximum aortic jet velocity, (ii) the mean transvalvular pressure and (iii) the aortic valve area always fit within the medical guidelines for the detection of the pathology and the assessment of the AS severity, see [39, 9]. Furthermore,

as reported in the last column of Table 1, the increase of ventricular pressure and aortic afterload induced by the AS yields a systematic reduction of the ejection fraction (EF). The latter, is an important clinical measure to quantify the heart pumping efficiency, which is defined as the ratio between the blood volume pumped by the left ventricle in a heart beat (stroke volume, SV) and the maximum ventricular volume (end diastolic volume, EDV). This observation can be rationalized recalling that in order to better investigate the effect of the AS, the same cardiac configuration is considered in normal and pathological cases. The mobility of the aortic valve leaflets, which is progressively reduced when modelling mild to severe AS (see section 2.1), is thus the only modification among the four cardiac simulations reported here. The contraction work produced by the active tension of the myocytes during systole is balanced by the mechanical work of the ventricular chamber (which is proportional to the stroke volume and pressure). Since the electrophysiology properties of the myocardium are not varied in the cardiac simulations, the total contraction work of the myocytes can be assumed to be about the same in healthy and pathological cases. As a consequence, since the cardiac pressure increase with the AS severity, the SV reduces, thus resulting in a lower EF, which reduces from 51% in the normal case to 47% (41%) in the mild (moderate) case up to 38% for severe AS.

3.3. Wall shear stress

The hemodynamics alterations originated by the AS have consequences also on the tissue wall shear stress (WSS), which is an important diagnostic parameter of the heart functioning being implied as a cause of disorders through mechanical hemolysis and tissue remodelling [36, 37]. The WSS are determined within the fluid solver and are defined as

$$\mathrm{WSS} = ||\mathbf{t_n} - (\mathbf{t_n} \cdot \mathbf{n})\mathbf{n}||, \tag{6}$$

where $\mathbf{n}$ is the unity vector normal to the surface, $\mathbf{t_n} = \boldsymbol{\tau} \cdot \mathbf{n}$ is the stress vector at the wall with $\boldsymbol{\tau}$ the viscous stress tensor (see section 2.2). Figure 7 shows

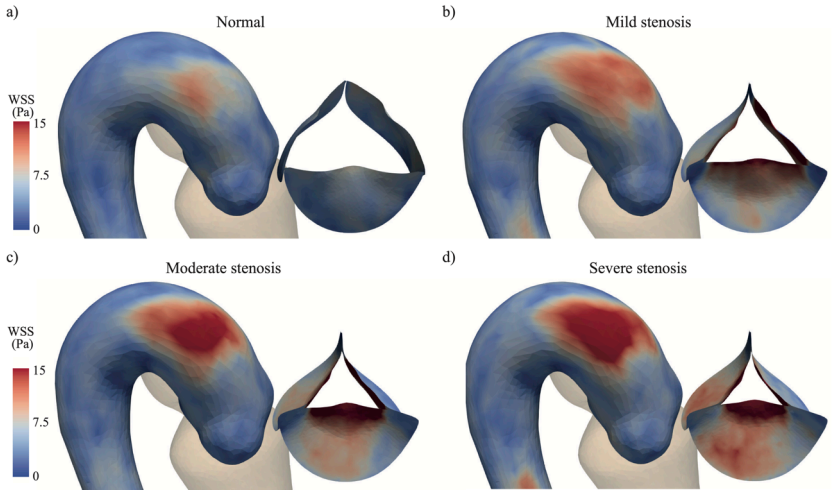

Figure 7: Distribution of the WSS over the aorta and aortic leaflets for (a) normal valve and (b) mild, (c) moderate, (d) severe AS. The size of the aortic valve and its position with respect to the left heart geometry has been modified for visualisation purposes.

the instantaneous WSS magnitude at the peak systole in the aorta and in the aortic valve leaflets as a function of the severity of the stenotic disease.

Regarding the aortic leaflets, in the non-stenotic case the WSS is always below 10 Pa with the highest WSS observed at their tips, where the shear layers detach and merge in the aortic jet. Moreover, this location corresponds to the minimum orifice area (and to the minimum section of the streamtube across the aortic valve) where the highest systolic velocities occur owing to mass conservation. Since blood velocity has to match the one of the valve leaflets at their surface (no-slip condition), thin boundary layers thus take place over the leaflets, corresponding to intense velocity gradients and, in turn, high WSS. For mild stenosis (panel b) the systolic jet flowing through the valve is faster than in the healthy case and, consequently, the WSS become more intense not only at the leaflets tip but also over the rest of their surface. The high WSS region further grows for moderate stenosis (panel c) until covering almost completely the leaflet surface for severe stenosis as reported in Figure 7d.

As already discussed in Figure 4, the systolic jet originated by the ventricular

contraction is directed vertically in the aorta and impinges the inner tissue of the aortic arch in the ascending part below its peak. In the case of healthy aortic valve this location has a small extension (see Figure 7a) and experiences a highest WSS of about 12 Pa. For mild (panel 7b) and moderate (panel 7c) AS, the region of high WSS spreads over the aortic arch, with maximum values of about 14 and 17 Pa, respectively. Figure 7d shows that in the case of severe stenosis, the systolic jet further narrows and accelerates, thus yielding more intense WSS over a large area of the aortic arch. The maximum WSS over this tissue is of 18 Pa, which corresponds to a net WSS increase of 50% with respect to the healthy case. A WSS increase from 10 to 18 Pa might appear inconsequential as the mechanical properties of the aortic tissue can certainly cope with it. However, the endothelium senses the abnormal value of the WSS and, in the medium- long-term, tissue remodelling is induced as a response to the pathological stimulus which produces irreversible changes in the structure and its functioning.

4. Discussion

In this work the effect of AS on the hemodynamics within the left heart is investigated through a state-of-the-art numerical model, which relies on the three way coupling among a Navier-Stokes solver, a structural solver (accounting for the orthotropic and hyperelastic tissue mechanics) and an electrophysiology solver (bidomain equations). Importantly, the expansion/contraction cycle of the heart chambers and the valve leaflets kinematic is not imposed but come as a part of the numerical solution. In particular, the AS induced by calcification is modelled in a similar fashion to [22] by preventing the mobility of a certain portion of the aortic leaflets close to the aortic root. The only control parameter of the AS model is the radius of the annular region identifying the calcific area, which is proportional to the severity of the pathology. In addition to the (i) normal case of healthy aortic valve (all portions of the valve leaflets can move), the model has been set so as to reproduce three different pathological configu-

rations, namely (ii) mild, (iii) moderate and (iv) severe stenosis. For each case, the cardiac dynamics has been solved in order to determine the perturbation in the hemodynamics induced by the valve pathology.

The numerical results evidence that our cardiac model not only predicts the correct trends of observable medical quantities as a function of the AS severity, but also provides data which are quantitatively consistent with the clinical experience [39, 9], as summarized in table 1. In particular, AS is seen to significantly alter the normal hemodynamics in terms of the blood velocity and pressure, especially during systole when blood is propelled towards the aorta through the aortic orifice by ventricular contraction. According to the numerical results, in the normal case with an AVA of 2.6 cm^2 the systolic jet has a velocity of 1.5 m/s at peak systole and a mean TPD during systole of 2.2 mmHg. In the stenotic case the systolic jet becomes faster and more irregular owing to the reduced mobility of the valve leaflets. In particular, the aortic jet velocity at peak systole increasing up to 2.6 m/s for mild stenosis and to 3.3 m/s for moderate stenosis, until getting to 4.9 m/s for severe stenosis (more than three times the velocity in case of normal valve). Accordingly, the mean TPD during systole increases from 12.7 to 42.5 mmHg as the stenosis severity is increased from mild to severe, with important implications on the transmural loads withstood by the heart chambers which are known to increase proportionally. These numerical results in the case of severe AS are in-line with the in-vitro experiments of [40], where a peak jet velocity of 4.9 m/s and mean TPD of 50 mmHg was observed for a HR of 70 bpm. Furthermore, the numerical simulations indicate that a normal cardiac configuration (i.e. with an EF $> 50\%$ according to medical standards [41]) turn to a *moderately reduced* EF (40-49%) with mild and moderate stenosis and to a *reduced* EF ($<40\%$) in the case of severe stenosis. It should be remarked, that these results correspond to the ideal scenario of a sudden and immediate occurrence of the pathology over a healthy heart, i.e. while keeping the other cardiac parameters unaltered. Such an approach neglects the long-term tissue remodelling induced by the pathology, where the perturbed hemodynamic loads applied to the endocardium are converted by the endothelial cells in biochemical

signals which regulate the electrical and mechanical modifications of the cardiac tissue [2, 38]. In the case of severe AS, the left ventricular myocardium generally gets weaken and enlarge, it looses contractility and further reduces the ventricle ability to pump blood, which become weak and dilated. This pathologic state, often induced by a prolongated AS, is known as *dilated cardiomyopathy* and it yields an increased risk of congestive heart failure. The study of these biologic process manifesting within a time scale of months/years is, clearly, out of the scope of the present work, where few heartbeats are solved through accurate numerical simulations.

A great advantage of the numerical approach proposed here is the possibility to quantify the alteration on the WSS induced by the AS, which can not be measured directly in-vivo. For both healthy and pathological cases, the highest WSS occur at the initial ascending tract where the aortic jet hits the inner artery wall, but as the stenosis gets more severe the narrower and faster systolic jet yields both an higher WSS level and a larger surface distribution. A similar trend is also observed on the surface of the valve leaflets where the WSS are normally more intense at their tips. As AS progresses the systolic flow accelerates, owing to a reduction of AVA and the region of high WSS gets not only more intense, but also spreads all over the surface of aortic leaflets including the annular outer region already calcified. In the case of severe stenosis, the augmented shear stresses and transient kinetic energy within the systolic phase can also damage red blood cells thus inducing platelet activations, which may leads to thromboembolic events arising from the formation of clots and their subsequent detachment [42, 43, 16]. These complications require lifelong anti-coagulation therapy, inducing high level of haemorrhage risk. Therefore, a natural continuation of this work would be to measure the damage of the red blood cells as a function of the AS severity by considering not only the Eulerian computation of the Reynolds stresses, but also tracking the trajectories of fluid particles to measure the instantaneous viscous stress tensor and the exposure time along their paths [16]. A Lagrangian approach would allow to better quantify the red blood cells damage and predict the onset of the hemolysis process as a function

of the severity of the stenotic disease. A possible improvement of the computational model would be to consider a non-uniform thickness distribution for the valve leaflets with a progressive increase of the tissue thickness approaching the calcific annular region of the valve. Furthermore, a simulation campaign could be run by varying the thickness and the stiffness of the valve leaflets, which are known to be correlated with the patient age, owing to a degeneration process of the collagen fibers and to lipid accumulation and calcification [44].

Acknowledgements

This project has received funding from the European Research Council (ERC) under the European Union's Horizon Europe research and innovation programme (grant agreement 101039657, CARDIOTRIALS to FV). CINECA is gratefully acknowledged for the access to high performance computing resources under the computational grant IsB23-CaRdiopT.

Conflict of interest

None.

References

1. J. E. Hall, Guyton and Hall textbook of medical physiology, Elsevier Health Sciences, 2010.
2. L. S. Lilly, E. Braunwald, Braunwald's heart disease: a textbook of cardiovascular medicine, volume 2, Elsevier Health Sciences, 2012.
3. F. Auricchio, M. Conti, S. Morganti, P. Totaro, A computational tool to support pre-operative planning of stentless aortic valve implant, Medical engineering & physics 33 (2011) 1183–1192.
4. B. A. Carabello, W. J. Paulus, Aortic stenosis, The lancet 373 (2009) 956–966.

5. C. A. Conti, E. Votta, A. Della Corte, L. Del Viscovo, C. Bancone, M. Cotrufo, A. Redaelli, Dynamic finite element analysis of the aortic root from mri-derived parameters, Medical engineering & physics 32 (2010) 212–221.

6. V. T. Nkomo, J. M. Gardin, T. N. Skelton, J. S. Gottdiener, C. G. Scott, M. Enriquez-Sarano, Burden of valvular heart diseases: a population-based study, The Lancet 368 (2006) 1005–1011.

7. N. M. Rajamannan, R. O. Bonow, S. H. Rahimtoola, Calcific aortic stenosis: an update, Nature clinical practice Cardiovascular medicine 4 (2007) 254–262.

8. C. W. Tsao, A. W. Aday, Z. I. Almarzooq, A. Alonso, A. Z. Beaton, M. S. Bittencourt, A. K. Boehme, A. E. Buxton, A. P. Carson, Y. Commodore-Mensah, et al., Heart disease and stroke statistics?2022 update: A report from the american heart association, Circulation (2022) CIR0000000000001052–CIR0000000000001052.

9. H. Baumgartner, J. Hung, J. Bermejo, J. B. Chambers, A. Evangelista, B. P. Griffin, B. Iung, C. M. Otto, P. A. Pellikka, M. Quiñones, Echocardiographic assessment of valve stenosis: Eae/ase recommendations for clinical practice, Journal of the American Society of Echocardiography 22 (2009) 1–23.

10. E. J. Weinberg, M. R. K. Mofrad, A multiscale computational comparison of the bicuspid and tricuspid aortic valves in relation to calcific aortic stenosis, Journal of biomechanics 41 (2008) 3482–3487.

11. R. Halevi, A. Hamdan, G. Marom, M. Mega, E. Raanani, R. Haj-Ali, Progressive aortic valve calcification: three-dimensional visualization and biomechanical analysis, Journal of biomechanics 48 (2015) 489–497.

12. Q. Wang, E. Sirois, W. Sun, Patient-specific modeling of biomechanical interaction in transcatheter aortic valve deployment, Journal of biomechanics 45 (2012) 1965–1971.

13. F. Sturla, M. Ronzoni, M. Vitali, A. Dimasi, R. Vismara, G. Preston-Maher, G. Burriesci, E. Votta, A. Redaelli, Impact of different aortic valve calcification patterns on the outcome of transcatheter aortic valve implantation: a finite element study, Journal of biomechanics 49 (2016) 2520–2530.

14. M.-C. Hsu, D. Kamensky, Y. Bazilevs, M. S. Sacks, T. J. Hughes, Fluid–structure interaction analysis of bioprosthetic heart valves: significance of arterial wall deformation, Computational mechanics 54 (2014) 1055–1071.

15. M.-C. Hsu, D. Kamensky, F. Xu, J. Kiendl, C. Wang, M. C. Wu, J. Mineroff, A. Reali, Y. Bazilevs, M. S. Sacks, Dynamic and fluid–structure interaction simulations of bioprosthetic heart valves using parametric design with t-splines and fung-type material models, Computational mechanics 55 (2015) 1211–1225.

16. M. De Tullio, A. Cristallo, E. Balaras, R. Verzicco, Direct numerical simulation of the pulsatile flow through an aortic bileaflet mechanical heart valve, Journal of Fluid Mechanics 622 (2009) 259.

17. M. D. De Tullio, L. Afferrante, G. Demelio, G. Pascazio, R. Verzicco, Fluid-structure interaction of deformable aortic prostheses with a bileaflet mechanical valve, Journal of biomechanics 44 (2011) 1684–1690.

18. H. G. Bahraseman, E. M. Languri, N. Yahyapourjalaly, D. M. Espino, Fluid-structure interaction modeling of aortic valve stenosis at different heart rates, Acta of bioengineering and biomechanics 18 (2016).

19. C. Zhu, J.-H. Seo, R. Mittal, Computational modelling and analysis of haemodynamics in a simple model of aortic stenosis, J. Fluid Mech 851 (2018) 23–49.

20. W. A. Zoghbi, M. Enriquez-Sarano, E. Foster, P. A. Grayburn, C. D. Kraft, R. A. Levine, P. Nihoyannopoulos, C. M. Otto, M. A. Quinones, H. Rakowski, et al., Recommendations for evaluation of the severity of

native valvular regurgitation with two-dimensional and doppler echocardiography, Journal of the American Society of Echocardiography 16 (2003) 777–802.

21. F. De Vita, M. D. de Tullio, R. Verzicco, Numerical simulation of the non-newtonian blood flow through a mechanical aortic valve, Theoretical and Computational Fluid Dynamics 30(1) (2016) 129–138.

22. V. Meschini, F. Viola, R. Verzicco, Modeling mitral valve stenosis: A parametric study on the stenosis severity level, Journal of biomechanics (2019).

23. V. Meschini, M. De Tullio, G. Querzoli, R. Verzicco, Flow structure in healthy and pathological left ventricles with natural and prosthetic mitral valves, Journal of fluid mechanics 834 (2018) 271–307.

24. F. Viola, V. Meschini, R. Verzicco, Fluid–structure-electrophysiology interaction (fsei) in the left-heart: A multi-way coupled computational model, European Journal of Mechanics-B/Fluids 79 (2020) 212–232.

25. D. A. Fedosov, B. Caswell, G. E. Karniadakis, Systematic coarse-graining of spectrin-level red blood cell models, Computer Methods in Applied Mechanics and Engineering 199 (2010) 1937–1948.

26. M. D. De Tullio, Pascazio, A moving-least-squares immersed boundary method for simulating the fluid-structure interaction of elastic bodies with arbitrary thickness, to appear in Journal of Computational Physics (2016).

27. Y. Kantor, D. R. Nelson, Phase transitions in flexible polymeric surfaces, Physical Review A 36 (1987) 4020.

28. M. Vanella, E. Balaras, A moving–least–squares reconstruction for embedded–boundary formulations, Journal of Computational Physics 228(18) (2009) 6617–6628.

29. E. P. van der Poel, R. Ostilla-Mónico, J. Donners, R. Verzicco, A pencil distributed finite difference code for strongly turbulent wall-bounded flows, Computers & Fluids 116 (2015) 10–16.

30. F. Viola, V. Spandan, V. Meschini, J. Romero, M. Fatica, M. D. de Tullio, R. Verzicco, Fsei-gpu: Gpu accelerated simulations of the fluid–structure–electrophysiology interaction in the left heart, Computer physics communications 273 (2022) 108248.

31. L. Tung, A bi-domain model for describing ischemic myocardial dc potentials., Ph.D. thesis, Massachusetts Institute of Technology, 1978.

32. J. Sundnes, G. T. Lines, X. Cai, B. F. Nielsen, K.-A. Mardal, A. Tveito, Computing the electrical activity in the heart, volume 1, Springer Science & Business Media, 2007.

33. K. ten Tusscher, A. Panfilov, Cell model for efficient simulation of wave propagation in human ventricular tissue under normal and pathological conditions, Physics in Medicine & Biology 51 (2006) 6141.

34. U. Arslan, M. Özdemir, S. A. Kocaman, S. Balcıoğlu, M. Cemri, A. Çengel, Heart rate variability and heart rate turbulence in mild-to-moderate aortic stenosis, Europace 10 (2008) 1434–1441.

35. M. P. Nash, A. V. Panfilov, Electromechanical model of excitable tissue to study reentrant cardiac arrhythmias, Progress in biophysics and molecular biology 85 (2004) 501–522.

36. D. G. Guzzardi, A. J. Barker, P. Van Ooij, S. C. Malaisrie, J. J. Puthumana, D. D. Belke, H. E. Mewhort, D. A. Svystonyuk, S. Kang, S. Verma, et al., Valve-related hemodynamics mediate human bicuspid aortopathy: insights from wall shear stress mapping, Journal of the American College of Cardiology 66 (2015) 892–900.

37. J. T. Butcher, R. M. Nerem, Valvular endothelial cells regulate the phenotype of interstitial cells in co-culture: effects of steady shear stress, Tissue engineering 12 (2006) 905–915.

38. V. Y. Wang, J. R. Hussan, H. Yousefi, C. P. Bradley, P. J. Hunter, M. P. Nash, Modelling cardiac tissue growth and remodelling, Journal of Elasticity 129 (2017) 283–305.

39. R. A. Nishimura, C. M. Otto, R. O. Bonow, B. A. Carabello, J. P. Erwin, L. A. Fleisher, H. Jneid, M. J. Mack, C. J. McLeod, P. T. O'Gara, et al., 2017 aha/acc focused update of the 2014 aha/acc guideline for the management of patients with valvular heart disease: a report of the american college of cardiology/american heart association task force on clinical practice guidelines, Journal of the American College of Cardiology 70 (2017) 252–289.

40. H. Maleki, S. Shahriari, M. Labrosse, P. Pibarot, L. Kadem, An in vitro model of aortic stenosis for the assessment of transcatheter aortic valve implantation, Journal of Biomechanical Engineering 136 (2014) 054501.

41. K. Kayama, T. Yamada, T. Watanabe, T. Morita, Y. Furukawa, S. Tamaki, M. Kawasaki, A. Kikuchi, T. Kawai, M. Seo, J. Nakamura, M. Kawahira, M. Fukunami, Comparative prognostic impact of ACCI and AHEAD risk score in heart failure with reduced, mid-range and preserved left ventricular ejection fraction admitted for acute decompensated heart failure, European Heart Journal 41 (2020).

42. R. L. Smith, E. F. Blick, J. Coalson, P. D. Stein, Thrombus production by turbulence, Journal of applied physiology 32 (1972) 261–264.

43. P. D. Stein, H. N. Sabbah, Measured turbulence and its effect on thrombus formation, Circulation Research 35 (1974) 608–614.

44. Y. Sahasakul, W. D. Edwards, J. M. Naessens, A. J. Tajik, Age-related changes in aortic and mitral valve thickness: implications for two-dimensional echocardiography based on an autopsy study of 200 normal human hearts, The American journal of cardiology 62 (1988) 424–430.